The DOI for this manuscript is doi: 10.1175/JCLI-D-17-0554.1

Deng, K., M. Ting, S. Yang, and Y. Tan, 2018: Increased Frequency of Summer Extreme Heat Waves over Texas Area Tied to the Amplification of Pacific Zonal SST Gradient. J. Climate. doi:10.1175/JCLI-D-17-0554.1, in press.

Increased Frequency of Summer Extreme Heat Waves over Texas Area Tied to the Amplification of Pacific Zonal SST Gradient

Kaiqiang Deng[1, 2]*, Mingfang Ting[2], Song Yang[1, 3, 4] and Yaheng Tan[1]

[1] *School of Atmospheric Sciences, Sun Yat-sen University, Guangzhou, China*

[2] *Lamont-Doherty Earth Observatory, Columbia University, Palisades, New York, USA*

[3] *Guangdong Province Key Laboratory for Climate Change and Natural Disaster Studies, Sun Yat-sen University, Guangzhou, China*

[4] *Institute of Earth Climate and Environment System, Sun Yat-sen University, Guangzhou, China*

Revised to *Journal of Climate*

April 2018

**Corresponding author address*: Kaiqiang Deng, School of Atmospheric Sciences, Sun Yat-sen University, 135 West Xingang Road, Guangzhou 510275, China. E-mail: dengkq@mail2.sysu.edu.cn

ABSTRACT

Summer extreme heat waves (EHWs) over Texas area and their trend are investigated using observations and atmospheric general circulation model (AGCM) outputs. There is a positive linear trend in Texas EHW days for the period of 1979-2015. While the interannual variability of the Texas EHWs is linked to ENSO conditions, the upward trend in Texas EHWs is found to be significantly associated with the tropical Pacific Zonal SST Gradient (PZSSTG). The amplification of PZSSTG leads to both enhanced convection in the western Pacific and suppressed convection in the central-eastern Pacific (i.e., La Niña-like pattern), both of which can induce anomalous anticyclones over the Texas area through two distinct planetary wave trains in the antecedent spring. As a result, anomalously sinking motions and divergent water vapor flux appear over the Texas area, which reduce precipitation and increase downward solar radiation, leading to a dry and hot soil that favors the occurrence of Texas summer EHWs. In addition, all AGCMs using observed SSTs as boundary conditions were able to simulate the observed decreasing trend in Texas summer precipitation and the observed increasing trend in Texas summer surface air temperature. The observed relationships between winter PZSSTG and the following spring-summer Texas precipitation/temperature were also reproduced by these models, where the intensified PZSSTG tended to reduce the Texas precipitation while increasing the surface air temperature.

1. Introduction

Texas and its surrounding areas have experienced numerous extreme heat waves (EHWs) over the past decades, which have produced large impacts on human health, agricultural productions, and natural ecosystem. For example, an EHW swept the central and southern United States in 1980, causing 107 heat-related deaths in Texas (Karl and Quayle 1981; Greenberg et al. 1983). In 1998, a more localized EHW struck Texas and Oklahoma that led to an estimated loss of 6 billion US dollars primarily due to decreased agricultural production (Chenault and Parsons 1998; Hong and Kalnay 2000). In 2011, an unprecedented EHW occurred over the Texas area, with an average temperature almost 3°C above the 1981–2010 mean for June through August (Nielsen-Gammon 2012; Hoerling et al. 2013), which substantially increased the emergency department visits for heat-related illnesses (Zhang et al. 2015). Among these cases, the 2011 EHW was the most notable in both intensity and duration, and was accompanied by a record-breaking burned area in the southern and southwestern Texas due to wildfires (Williams et al. 2014). Smith et al. (2013) indicated that the EHW frequency, in terms of EHW days per year, over southern North America, experienced an upward trend based on the various EHW definitions. More intense and longer lasting EHWs over the Texas area have raised concerns of the potential impact of greenhouse warming on the increasing frequency of Texas EHWs.

The potential mechanisms associated with EHWs include the precipitation – evaporation – temperature feedback (e.g., Fischer et al. 2007; Lorenz et al. 2010; Mueller and Seneviratne 2012) and persistent anticyclones or blocking highs (e.g., Dole et al. 2011;

Trenberth and Fasullo 2012; Screen and Simmonds 2014). Both of these can be triggered or forced by the remote sea surface temperature anomalies (SSTAs) or internal atmospheric dynamics. For example, Hong and Kalnay (2000) found that the Pacific SSTAs could establish large–scale conditions for Texas drought during the antecedent spring through atmospheric teleconnection. The spring soil moisture anomalies subsequently play an important role in maintaining the drought and triggering the summer EHWs by a positive feedback associated with lower evaporation/precipitation. On the other hand, Lyon and Dole (1995) analyzed the large–scale circulations associated with the Texas EHW in 1980, and found that this particular event was primarily forced by a stationary wave propagating southeastward from an apparent source region south of the Aleutians. Using an atmospheric general circulation model (AGCM), Teng et al. (2013, 2016) indicated that the EHWs in the United States tend to be preceded by a pattern of anomalous atmospheric planetary waves with a wavenumber of 5 by 15–20 days. Petoukhov et al. (2013) further noted that the 2011 Texas EHWs were significantly connected with the planetary waves with zonal wavenumbers 6, 7, or 8 that are trapped within the mid-latitude waveguide. Screen and Simmonds (2014) also proposed that the amplification of quasi-stationary waves with zonal wavenumbers 3–8 preferentially increases the probability of EHWs in North America.

Other studies have compared the roles of greenhouse warming and oceanic forcing in affecting the drought/heat waves in Texas area. Using an AGCM, Rupp et al. (2012, 2015) investigated the influence of anthropogenic greenhouse warming on the Texas EHW in 2011 and concluded that the likelihood of exceeding a given unusually high summer temperature in the Texas region was about 10 times greater with 2011 anthropogenic emissions compared to pre-industrial forcing. Furthermore, Rupp et al. (2013, 2017) assessed the influences of greenhouse gases and ocean's role for the 2012 central United States drought and found that the SSTAs, rather than the anthropogenic forcing, were more likely to increase the occurrence of the 2012 drought/heat. Wang et al. (2014) compared the roles of SST forcing in the 2011 and 2012 drought and heat events in the United States using the NASA Goddard Earth Observing System version 5 (GEOS5) AGCM, and found that the winter/spring responses over the United States to the Pacific SSTAs were remarkably similar for these two years despite substantial differences in the tropical Pacific SST, implying that the SSTAs outside the central and eastern Pacific might also play some roles.

It is well known that precipitation deficits in southern and southwestern North America are linked to the tropical Pacific SSTA, notably to the cold state of the eastern Pacific, which usually leads to anticyclonic anomalies over these regions that favor high pressures and dry conditions (e.g., Schubert et al., 2004; Seager and Ting 2017). However, there is no conclusive evidence showing whether La Niña activities have been enhanced or damped in recent decades due to the relatively small samples of the ENSO events (Collins et al. 2010). Thus ENSO alone may not be sufficient to explain the increasing Texas EHWs.

Hoerling and Kumar (2003) linked the drought/heat in the United States to the cooling in the eastern tropical Pacific and the warming in the western Pacific. The warmth of the Indo-Pacific oceans has been unprecedented in recent decades, accompanied by an enhanced Pacific Zonal SST Gradient (PZSSTG) (L'Heureux et al. 2013; McGregor et al. 2014). A strengthened PZSSTG, on the one hand, favors the cold state maintenance in the central – eastern Pacific, which can induce robust anticyclones over southern North America and the occurrence of EHWs. On the other hand, the intensified PZSSTG can also enhance convective activities in the western tropical Pacific, which may also affect the North American EHWs through teleconnection. Thus, it is of interest to determine the possible impacts of ENSO and the PZSSTG on the increasing trend in Texas EHWs and to explore the underlying mechanisms.

In the current study, the trend and year-to-year variability in Texas EHWs are investigated. We also compare the different physical processes associated with ENSO and PZSSTG, focusing mainly on the tropical western Pacific. The rest of the paper is organized as follows. In section 2, we describe the data sets and analysis methods. In section 3, we discuss the overall features of EHWs in North America. In section 4, we explore the drivers and associated mechanisms. The AGCM simulated results are discussed in section 5, followed by a summary in section 6.

2. Data and Method

a. Observations and model outputs

For comparison purposes, we use two sets of data for SST, precipitation, and maximum 2-m temperature (Mx2t). The monthly mean SST data sets are obtained from the National Oceanic and Atmospheric Administration (NOAA) extended reconstructed version 4 (NOAA–ERAv4; Huang et al. 2015) and the Hadley Centre (HadISST, Rayner et al. 2003), with horizontal resolutions of 2°×2° and 1°×1°, respectively. The land precipitation data sets are acquired from the Global Precipitation Climatology Centre (GPCC; Schneider et al. 2011) and the European Centre for Medium-Range Weather Forecasts (ECMWF) ERA-Interim (Dee et al. 2011), both having a horizontal resolution of 0.5°×0.5°. The daily Mx2t data sets are used to define EHWs, which are obtained from the ECMWF ERA-Interim (Dee et al. 2011) and the NCEP-DOE Reanalysis 2 (provided by the NOAA/OAR/ESRL PSD, Boulder, Colorado, USA; their Web site: http://www.esrl.noaa.gov/psd/), with a resolution of 0.5°×0.5° and a global T62 Gaussian grid (192×94), respectively. For most figures, the Texas EHWs and their relations with other variables are shown based on the ERA-Interim data.

The atmospheric variables, including geopotential height, three-dimensional velocity at 17 levels, the 4-layer volumetric soil moisture, and the vertical integrals of eastward and northward moisture fluxes, are used to diagnose the associated large-scale conditions for the variation in EHWs. These data sets, with a horizontal resolution of 2.5°×2.5°, are also obtained from the ECMWF ERA-Interim (Dee et al. 2011). The Niño3.4 index is defined as the area-averaged SSTAs over the central and eastern Pacific (170°E–120°W, 5°S–5°N) based on the NOAA-ERV4 data. The PZSSTG is computed from the NOAA-ERV4 SSTA differences between the tropical western Pacific (120°E–150°E, 10°S–10°N) and Niño3.4. The analysis period in this study is 1979–2015.

To assess the impacts of ENSO and PZSSTG on Texas precipitation and temperature, we analyze the outputs from several AGCMs provided by the NOAA Drought Task Force (DTF; Schubert et al., 2009). The reason these DTF experiments were chosen here is that the models tend to have good skill at simulating different drought mechanisms, feedbacks, and potential predictability of several high-profile cases (Wood et al. 2015). These cases include the southeastern U.S. drought during 2006/07, the Texas drought of 2011, the central Great Plains drought of 2012, and the western U.S. drought from 1998 to 2002. The model outputs used in this study are from the AGCM experiments forced by observed SST for the period of 1979–2014. The models are ECHAM5, CFSv2, CAM4, GEOS5, and CCM3, whose horizontal resolutions are 0.75°×0.75°, 1°×1°, 1.25°×0.75°, 1.25°×1°, and 2.5°×2.5°, respectively. Each AGCM produced 12-20 ensemble members. We calculate the ensemble means for each model before analyzing the results.

b. EHW thresholds and EHW days

The EHWs are defined by a percentile–based threshold method, which is widely used (e.g., Meehl and Tebaldi 2004; Della–Marta et al. 2007; Kuglitsch et al. 2010). For a specific day within the June–August period, its maximum temperature threshold is determined by the 95^{th} percentile of Mx2t for a total of 555 days (37 years × 15 days, the 15 days correspond to 7 days on either side of the target date) for the 37-year period from 1979 to 2015. By moving the 15-day window forward or backward, we get the consecutive threshold for every target date. An EHW event is identified by two criteria: (1) there are at least 3 consecutive days that the Mx2t exceeds its 95^{th} percentile threshold, and (2) the average Mx2t during the EHW event must exceed 30°C. Therefore, the EHW days (EHWD) can be acquired by computing the total days of EHWs over a specific period (an example is given in Fig. 2c for the 2011 summer in Texas). A large EHWD represents that there are more threshold-breaking hot days or more frequent EHWs, and vice versa.

In addition, we also use the singular value decomposition (SVD) method to explore the relationship between Pacific SSTAs and North American EHWD, which allows us to identify their covariability (Bretherton et al. 1992). In sections analyzing the interannual variability in Texas EHWs, the linear trends and low-frequent signals in Texas EHWs are removed by the 10-year running mean method. The statistical significances of the composite and correlation results are tested by the two-tailed Student's *t*-test, with a degree of freedom of 35 for a total of 37 years (1979–2015).

3. Characteristics of EHWs over North America

Figure 1a shows the climatological patterns of North American Mx2t and 500-hPa geopotential height averaged for the boreal summer (JJA). We can see that there exist two high temperature centers, which are located over southwestern and south–central North America, where Mx2t exceeds 33°C. The hot regions coincide with the subtropical anticyclone, which stretches from the subtropical North Atlantic to the eastern Pacific. It is well understood that a subtropical high is often accompanied by descending air motion, less precipitation, and clear skies, thus resulting in high daily maximum temperature.

Figure 1b presents the total EHWD in North America during JJA for the period 1979–2015. In general, the relatively high value of EHWDs can be found over western, southwestern, and south-central North America, compared to the northern and eastern regions. Such distribution is expected given the North American climate landscape of dry west–wet east as well as the frequently reported droughts over the regions with large EHWDs (e.g., Yin et al. 2014; Rupp et al. 2015). The largest values of EHWD seem to appear over

Texas/Oklahoma areas, where there are more than 80 summer days (out of 3404 days) during JJA when the Mx2t exceeds the EHW threshold.

The linear trend in EHWD is shown in Fig. 1c. Although strong EHW activities exist over western North America, the trend there is insignificant. In comparison, the largest trend in EHWD is clearly seen over Texas and its nearby areas, which is significant at the 95% confidence level. The EHWD trends shown in Fig. 1c are consistent with many previous studies (e.g., Lau and Nath 2012; Smith et al. 2013; Teng et al. 2016), which reported that the largest trends in EHWD occurred in southeastern North America and the Great Plains. However, these studies did not address why the largest trend in EHWD appeared in the Texas area. Therefore it is our goal here to determine why the Texas areas seem to be the preferred locations of increasing EHWs and what are the underlying mechanisms?

To answer these questions, we further investigate the year–to–year variations of Texas EHWs and associated atmospheric and oceanic conditions. Figure 2a shows the area-averaged EHWD over the domain (105°W–90°W, 28°N–38°N) based on both 90% and 95% thresholds over the 37 years. While large interannual variation exists in the Texas EHWD, the 10–year running mean (dashed line) seems to indicate a consistent upward trend from 1979 to 2015. The largest EHWD was found in 2011, which has been recognized as one of the most extreme summers (e.g., Zhou et al. 2014; Rupp et al. 2015; Zhang et al. 2015). As a way to remove the trend and focus on interannual variation, we identified 10 years when the values of EHWD exceeded the 10-year running mean (i.e., 1980, 1986, 1989, 1996, 1998, 2000, 2006 2009, 2011, and 2012, see supplementary Fig. S1 for each year's EHW Days spatial patterns), as marked in Fig. 2a. These 10 years are selected to make the composite analysis next.

Figure 2b shows the monthly Niño3.4 index and area-averaged precipitation for Texas and surrounding area (105°W–90°W, 28°N–38°N, blue box in Fig. 1c), from January 1979 to December 2015. The 10 severe EHW summers are indicated by the black triangles in Fig. 2b, which correspond well with the central and eastern Pacific SST cooling during the preceding winter and spring. Further examinations reveal that most winters (8 out of 10) preceding the Texas summer EHWs are featured by anomalously cold SSTAs in the central and eastern Pacific, except for the 1979/80 and 1997/98 winters (See supplementary Fig. S2). As seen from Fig. 2b, large precipitation deficits are also found preceding each occurrence of Texas EHWs. In fact, Texas precipitation and Niño3.4 are well correlated for all months from January 1979 to December 2015, with a correlation coefficient of 0.47, suggesting that the central and eastern Pacific cooling can lead to significant rainfall deficit in spring and summer, which further lead to drought in the Texas region in the summer (Seager and Hoerling 2014).

The 2011 summer is seen as the case with the most extreme EHWD for the entire study period, which follows a strong La Niña event with reduced spring and summer Texas precipitation (Fig. 2b). We show in Fig. 2c a selected site (98°W, 34°N), which is a grid cell near Wichita Falls, Texas, to illustrate the evolution of this extreme case based on ERA-Interim data. As can be seen, the 95th threshold temperature is generally lower in the beginning and the end of the summer, and peaks in mid-summer. Most of the dates above the 95% thresholds during this summer were between mid-June and late-August, when there were consecutive days with maximum Mx2t exceeding 40°C (104°F).

To determine statistically whether the increase in Texas daily Mx2t was simply due to the background warming (thus a shift of the mean Mx2t) or it might involve additional processes, Fig. 3a shows the probability density function (PDF) of Texas daily Mx2t for the 10 extreme summers (red), the rest of the 27 summers (grey), the first half of the period from 1980-97 (blue) and the second half of the period from 1998 to 2015 (cyan). The PDFs for the two different periods (blue vs. cyan) show a clear shift due to changes in the mean, from 32°C in the first half to 35°C in the second half, which could reflect a global warming contribution or the Pacific/Atlantic multi-decadal modulation (McCabe et al. 2004) to the Texas EHWs. The PDF for the 10 extreme summers, however, show a more dramatic increase in probability of the high daily Mx2t compared to all three other PDFs in Fig. 3a. Compared to the normal years, i.e., the rest of the 27 years, the possibility of occurrence of Mx2t above 35°C is much higher in these 10 extreme summers. In particular, the probability of occurrence of Mx2t between 36°–39°C is substantially higher in extreme summers. Thus, the increased EHWs in the Texas area could be affected not only by the shift in mean temperature, but could be also influenced by additional processes involved in causing these extremes. In Fig. 3b, we illustrate that the seasonal mean Mx2t and the EHWD averaged over the Texas area are highly correlated with a correlation coefficient of 0.87. This linear relationship is more evident for the 10 EHWs summers. Therefore, in cases when daily Mx2t is not available, it is an alternative method to use the seasonal mean surface temperature to represent EHWs in the Texas area.

4. Drivers and mechanisms associated with Texas EHWs

a. Relationship between Pacific SSTA and Texas EHW

It is clear from Fig. 2b that there is a strong relation between Texas EHW and SSTA in the tropical Pacific. Figure 4 explores this relationship further by compositing tropical Pacific SSTAs and 200-hPa geopotential height in the preceding winter, spring, and simultaneous summer based on the 10 most EHW events of Texas. We can see that warming and cooling SSTAs appear in the western and central Pacific, respectively, resembling the mature and decaying La Niña patterns from winter to summer. Correspondingly, as shown in the right panels of Fig. 4, stationary Rossby waves are triggered in the upper troposphere, which originate from the central Pacific and propagate poleward. The stationary waves branch out in two directions over the North Pacific, one continuing across the Arctic region and dissipating in the eastern hemisphere, and the other turning southeastward in both winter and spring. By the spring season, an anomalous high pressure is found over the Texas area, which persists into the summer season.

The precipitation and vertically-integrated water vapor flux (WVF) composites for the EHW years are shown in Fig. 5, for both the spring and summer seasons. During the antecedent spring, the westward and eastward WVF anomalies prevail over the subtropical and mid–latitude regions, respectively, due to the anomalous atmospheric anticyclones, which results in significant precipitation deficit in southern North America. During summer, the divergent WVF anomalies intensified, and were accompanied by anomalous southward WVF leading to widespread precipitation deficit in Texas and its surrounding regions.

The results in Figs. 4 and 5 suggest a plausible mechanism for the Texas EHWs under

La Niña conditions. A La Niña event first causes anomalous downstream stationary wave propagation, which induces anticyclonic anomalies over the Texas area in spring and summer. The anomalous anticyclone then reduces cloud cover and precipitation, which leads to drier soils, and thus fosters more EHWs there (Hong and Kalnay 2000). It is, however, unclear if the La Niña SSTAs could have caused the increasing trend in Texas EHWs. Previous studies indicated that the PZSSTG had intensified over the past three decades, which was accompanied by the recent strengthening of the Pacific Walker circulation (e.g., Kosaka and Xie 2013; McGregor et al. 2014). Is the increasing trend in Texas EHWs the result of intensified PZSSTG or purely due to La Niña conditions?

To answer this question, Fig. 6 shows the time series of the PZSSTG and Niño3.4, as well as their relations with Texas precipitation. We can see that the PZSSTG presents a significant strengthening trend in both ERSST and HadiSST data sets, while the trend in Niño3.4 is small and insignificant, implying that the western Pacific SST warms faster than that in the central and eastern Pacific in observations. As shown in Figs. 6c and 6e, the intensification of PZSSTG tends to significantly decrease the spring and summer precipitation over the Texas area. The correlation coefficient between antecedent winter PZSSTG and the following spring (summer) Texas precipitation reaches -0.45 (-0.40), exceeding the 99% (95%) confidence level. As a special case, the precipitation anomaly during the 2011 summer is marked in Fig. 6e, which coincided with the largest PZSSTG.

In comparison, the scatter plots between Texas precipitation and the Niño3.4 index are shown in the right panels of Fig. 6. The correlation between Texas precipitation and the winter Niño3.4 index decreases from -0.45 to -0.33 (from -0.40 to -0.36) during the boreal spring (summer), though still significant above the 95% confidence level. The 2011 case is marked in Fig. 6f, showing the Texas precipitation deficit corresponded to a moderately large Niño3.4 value, but not the strongest La Niña.

Figure 7 further shows the relationships between DJF PZSSTG (Niño3.4) and Texas area soil water and between DJF PZSSTG (Niño3.4) and Mx2t. It should be noted that although significant linkages between these variables are found, the uncertainties in these values are relatively large, especially for the soil water provided by ERA-Interim. Therefore, one should be more cautious in explaining these correlation relationships. The summer Texas soil water shows a significantly negative correlation with the winter PZSSTG, with a correlation coefficient of -0.42, which could be related to the precipitation deficits in previous seasons. Figure 7c shows that the Texas Mx2t tends to increase corresponding to the amplification of DJF PZSSTG, which likely results from the precipitation – soil moisture – temperature feedback (Schär et al. 1999; Fischer et al. 2007). The 2011 summer was extremely hot, which was accompanied by the largest precipitation deficit and dry soil condition. Similar to the Texas precipitation, the correlation coefficient between Niño3.4 and Texas soil water/Mx2t is less significant compared to that with PZSSTG. In fact, the correlation coefficient between DJF negative Niño3.4 (i.e., multiplied by -1) and Texas JJA Mx2t is only 0.29, which is below the 95% confidence level. Thus, although the DJF La Niña may play an important role in the occurrence of Texas summer EHWs, the western Pacific SSTAs can also contribute to some extent, which enhances the PZSSTG and the associated tropical convection.

b. Physical mechanisms associated with Texas EHW

How much can the Pacific SSTAs and associated convections explain the trend and variability of Texas EHWs? To answer this question, we performed Singular Value Decomposition (SVD) analysis between the Pacific outgoing longwave radiation (OLR) in DJF and the North American EHWD in the following summer (JJA) to extract the co-variability between tropical convection and extreme heat waves. The OLR is usually used to measure the convective intensity in the tropics, where a small (larger) OLR value indicates stronger (weaker) convection. As seen from Fig. 8a, the first SVD mode presents negative correlation in the western Pacific (WP), positive correlation in the central Pacific (CP), and negative correlation in the eastern Pacific (EP), implying enhanced convection over the WP and suppressed convection over the CP. Meanwhile, the OLR pattern is correlated with significant warming in the WP and cooling in the CP, implying an intensification of PZSSTG. It is well known that an intensified PZSSTG could drive a stronger Walker circulation in the equatorial Pacific, which favors the WP convection. Thus, the enhanced convection over the WP may be viewed as a response to the increased PZSSTG.

Correspondingly, the EHWD over most of the US, particularly in Texas and Oklahoma, increases (Fig. 8b), which accounts for 47.8% of the total covariance between OLR and EHWD. Figure 8c shows the time series of the first SVD mode for OLR and EHWD, both showing an upward trend, with a correlation coefficient of 0.63 between the two variables, indicating a direct link between enhanced convection over WP and the Texas EHWs. To better understand the dynamical linkage between WP convection and Texas EHWs, a WP

OLR index is constructed using the area–averaged OLR over the WP domain (100°E–130°E, 15°S–20°N).

The WP OLR and PZSSTG indices are shown in Fig. 9a. The WP OLR shows a significantly downward trend, implying that the WP convection became stronger in recent decades. In comparison, the PZSSTG shows a significantly increasing trend, which corresponds well with the decrease in WP OLR, with a high correlation coefficient of -0.78. To determine the atmospheric circulation features associated with the WP convection, we show in Fig. 9(b) the regression pattern of 200-hPa geopotential height onto the negative WP OLR index (i.e., multiplied by -1). Corresponding to the enhancement of WP convection, there exist two distinct Rossby wave trains. One originates from the central Pacific, similar to that shown in Fig. 4, which is likely triggered by ENSO SST anomalies. The other originates from the WP and propagates across the North Pacific, contributing to the anomalously high pressure over southern North America during boreal spring. After removing the ENSO signal by regressing out Niño3.4 from the WP OLR index, the Rossby waves originating from the central Pacific disappear almost completely (Fig. 9c), while the WP originated Rossby waves intensified. By comparing Figs. 9b and 9c, one can see clearly that both La Niña and the enhanced convection in the WP contribute to the anticyclones and thus EHWs over the southern United States.

The anomalous circulation pattern associated with WP OLR tends to persist to the summer (See supplementary Fig. S3), although the magnitude of the wave train weakens, which results in anomalous high pressure over the Texas area, leading to prolonged dry and hot conditions. The correlation coefficient between the spring (summer) Texas precipitation and the ENSO – removed negative WP OLR index is approximately -0.3 (-0.2), which is significant at the 90% (80%) confidence level. The summer Texas Mx2t also shows a positive relationship (0.28) with the ENSO – removed negative WP OLR index, which confirms the hypothesis that the WP convection may contribute to the occurrence of Texas EHWs through wave propagation, although the relationship is not as strong as the one including ENSO.

5. AGCM experiment results

Five AGCMs from the NOAA Drought Task Force simulations (Schubert et al., 2009) are used in this section to further examine the linkage between Texas climate and Pacific SST conditions. Forced by observed SST, these AGCMs simulated well the climatology of summer precipitation and 2-m temperature (T2m) over North America, with dry west–wet east pattern regardless of their different horizontal resolutions (see supplementary Fig. S4).

Figure 10 shows the ensemble means of precipitation and T2m averaged over the Texas area during the summer. All five AGCMs simulated a negative trend in Texas precipitation since 1990s and a positive trend in T2m. Due to the lack of daily model outputs, the EHWs cannot be defined in the same way as before. Instead, we use monthly mean T2m temperature to define extreme hot summers, a reasonable alternative considering the close relationship between seasonal mean Mx2t and EHWD as shown in Fig. 3b. The increasing trend in Texas summer T2m simulated by all models implies more frequent EHWs over Texas area in Fig. 10b. The correlation coefficient between the multi-model mean (MMM) T2m and precipitation in summer is as high as -0.9, indicating that the increase in Texas surface air temperature primarily results from the reduction in local precipitation. In comparison, the correlation coefficient between Texas surface air temperature and precipitation from the observation is -0.84, only slightly smaller than that from the model simulations. The small reduction in correlation is due to the larger atmospheric internal variability in observations as compared to the multi-model ensemble mean. The high correlation confirms that lower precipitation could lead to drier soil conditions and reduced evaporation, leading to higher surface temperature and less precipitation. In addition, the decreased precipitation is usually accompanied by fewer clouds and more surface solar radiation, which lead to a higher surface air temperature.

Figure 11 shows the regression maps of simulated spring 200-hPa geopotential height onto the antecedent winter PZSSTG. One of the most prominent features is the La Niña-forced wave pattern, showing anomalous low-pressure centers over the tropical Pacific and northern North America, and anomalously high-pressure centers over the North Pacific and southern North America. After linearly removing the ENSO signals, the WP-originated wave trains become more obvious, which propagate across the North Pacific and lead to anomalously high pressure over the Texas area. Note that substantial heterogeneity exists in the intensity and location of the simulated wave trains among different AGCMs, although the anomalous anticyclones over the Texas area were simulated by most AGCMs, implying that both the WP and EP SSTAs exert influences on Texas climate.

We further examine the relationships between Texas precipitation/temperature and PZSSTG/Niño3.4 within the AGCM framework. The left panels of Fig. 12 show that the winter PZSSTG has a negative correlation with the MMM precipitation over Texas during the following spring (summer), with a correlation coefficient of -0.82 (-0.73). The correlation coefficients between PZSSTG and Texas precipitation simulated by the AGCMs are much higher than that in observations, as expected from the multi-model mean that reduces atmospheric internal variability and emphasizes the SST-forced signal. Correspondingly, the PZSSTG shows a positive correlation with the MMM T2m over Texas during summer, with a correlation coefficient of 0.77. The AGCM results confirm that the amplification of winter PZSSTG tends to reduce precipitation and increase T2m over the Texas area.

The right panels of Fig. 12 show the similar scatter plots between Texas precipitation/temperature and negative Niño3.4 index. While the DJF SSTAs in the central–eastern Pacific also show significant relationships with Texas precipitation and temperature in the following spring and summer, the magnitudes of the correlation coefficients are much reduced compared with those for the PZSSTG. These results confirm again that the WP SSTAs and the associated wave trains contribute to the variability in precipitation and temperature over the Texas area.

6. Summary

This study investigated the trend and year-to-year variability in Texas extreme heat wave events. In climatology, the EHWs mainly occur over western, southwestern, and southern North America, as revealed by previous studies (e.g., Lau and Nath 2012; Smith et al. 2013; Teng et al. 2016). The largest trend of EHWs is found over the Texas area, which is found to be related to the enhanced tropical PZSSTG in the antecedent winter and spring. The enhanced PZSSTG can be a result of La Niña conditions, which lead to the cooling of eastern tropical Pacific and result in anticyclonic circulation anomalies over the Texas areas through planetary wave propagation. However, La Niña alone is found to be insufficient to explain the increasing trend in Texas EHWs, suggesting the possible contributions of the warming western tropical Pacific to the Texas EHWs.

The SVD analysis between tropical Pacific OLR and North American extreme heat wave days reveals that the WP convection associated with the amplification of PZSSTG is correlated with the increased frequency of Texas EHWs. In recent decades, the winter PZSSTG has experienced an increasing trend, consistent with the Texas EHWs. The winter PZSSTG also shows a significant correlation with the Texas precipitation in following spring (summer). In comparison, the correlation coefficients between Niño3.4 and the Texas precipitation/temperature in following spring and summer are weaker than that with the antecedent PZSSTG, suggesting that the warm WP SSTAs may contribute to the Texas EHWs.

The physical mechanisms linking the occurrences of Texas EHWs and the PZSSTG are found to be associated with two distinct wave trains. One is triggered by La Niña conditions and originates from the central tropical Pacific that propagates northeastward, leading to an anomalous anticyclone over the Texas area. The other originates from the western tropical Pacific and propagates northeastward across the North Pacific, which also contributes to the Texas high pressure anomaly. Although the La Niña related wave trains dominate the Texas climate, the WP originated wave trains add significantly to the relationships between

PZSSTG and the Texas climate. The increased PZSSTG favors the intensification of WP convection and the maintenance of stronger Pacific cooling, both of which contribute to the anticyclone anomalies over Texas area. Under the control of a persistent anticyclone, sinking air and clear skies prevail, which suppress the local convection and reduce precipitation. Through precipitation – soil moisture – temperature feedback, higher surface temperatures and the increased occurrences of EHWs are expected.

Our study points at the importance of the anomalous WP SSTAs and convection to the Texas spring and summer precipitation as well as the summer heat wave events. Previous studies (e.g., Kosaka and Xie 2013; McGregor et al. 2014) have found an enhanced PZSSTG as a result of greenhouse warming based on the coupled ocean–atmosphere model simulations, which would point to possible future increases in Texas heat wave occurrences and exacerbated drought in the region through atmosphere teleconnection. It should be cautioned that our study does not explicitly address the role of anthropogenic forcing in recent Texas droughts/heats. Rupp et al. (2015) indicated that no simulated increase in the frequency of large precipitation or soil moisture deficits was detected from preindustrial to year 2011 conditions. The dynamic mechanism proposed here could also apply to shorter time scales, such as the intraseasonal time scales, when the western tropical Pacific convection due to the Madden–Julian Oscillation (e.g., Barlow and Salstein 2006; Zhou et al. 2012) can trigger similar wave trains and lead to Texas heat waves.

Acknowledgments. The authors wish to thank Drs. Donna Lee, Deepti Singh, and Lei Wang at the Lamont – Doherty Earth Observatory for fruitful discussions. KD is supported by the China Scholarship Council while visiting Columbia University's Lamont-Doherty Earth Observatory. MT is supported by the National Science Foundation (EaSM2 grant AGS 12-43204) and the National Oceanic and Atmospheric Administration (grants NA10OAR4310137 and NA14OAR4310223). The study is also supported by the National Natural Science Foundation of China (grants 41690123 and 41690120), the Jiangsu Collaborative Innovation Center for Climate Change, and the Zhuhai Joint Innovative Center for Climate, Environment and Ecosystem.

REFERENCES

Barlow, M., and D. Salstein, 2006: Summertime influence of the Madden–Julian oscillation on daily rainfall over Mexico and Central America. *Geophys. Res. Lett.*, **33,** L21708.

Bretherton, C. S., C. Smith, and J. M. Wallace, 1992: An intercomparison of methods for finding coupled patterns in climate data. *J. Climate,* **5,** 541–560.

Chenault, E., and G. Parsons, 1998: Drought worse than 96; cotton crop's one of worst ever. http://agnews.tamu.edu/stories/AGEC/Aug1998a.htm, Texas A&M Agricultural News Home Page, College Station, TX, August 19.

Collins, M., and Coauthors, 2010: The impact of global warming on the tropical Pacific and El Niño. *Nat. Geosci.*, **3,** 391–397.

Dee, D. P., and Coauthors, 2011: The ERA-Interim reanalysis: Configuration and performance of the data assimilation system. *Quart. J. Roy. Meteor. Soc.*, **137,** 553–597.

Della-Marta, P. M., M. R. Haylock, J. Luterbacher, and H. Wanner, 2007: Doubled length of western European summer heat waves since 1880. *J. Geophys. Res.*, **112,** D15103.

Dole, R., and Coauthors, 2011: Was there a basis for anticipating the 2010 Russian heat wave? *Geophys. Res. Lett.,* **38,** L06702, doi:10.1029/2010GL046582.

Fischer, E. M., S. I. Seneviratne, P. L. Vidale, D. Lüthi, and C. Schär, 2007: Soil moisture–atmosphere interaction during the 2003 European summer heat wave. *J. Climate*, **20,** 5081–5099.

Greenberg, J., J. Bromberg, C. Reed, T. Gustafson, and R. Beauchamp, 1983: The epidemiology of heat-related deaths, Texas–1950, 1970–79, and 1980. *AJPH*, **73,** 805–

807.

Hoerling, M., and A. Kumar, 2003: The perfect ocean for drought. *Science*, **299,** 691–694.

Hoerling, M., and Coauthors, 2013: Anatomy of an extreme event. *J. Climate*, **26,** 2811–2832.

Hong, S. Y., and E. Kalnay, 2000: Role of sea surface temperature and soil-moisture feedback in the 1998 Oklahoma–Texas drought. *Nature,* **408,** 842–844.

Huang B., V. F. Banzon, E. Freeman, J. Lawrimore, W. Liu, T. C. Peterson, T. M. Smith, P. W. Thorne, S. D. Woodruff, and H.-M. Zhang, 2015: Extended Reconstructed Sea Surface Temperature version 4 (ERSST.v4). Part I: Upgrades and intercomparison. *J. Climate*, **28,** 911–930.

Karl, T. and R. Quayle, 1981: The 1980 summer heat wave and drought in historical perspective. *Mon. Weath. Rev.*, **109,** 2055–2073.

Kosaka, Y., and S.-P. Xie, 2013: Recent global-warming hiatus tied to equatorial Pacific surface cooling. *Nature*, **501,** 403–407.

Kuglitsch, F. G., A. Toreti, E. Xoplaki, P. M. Della-Marta, C. S. Zerefos, M. Türkeş, and J. Luterbacher, 2010: Heat wave changes in the eastern Mediterranean since 1960. *Geophys. Res. Lett.*, **37,** L04802.

Lau, N.-C., and M. J. Nath, 2012: A model study of heat waves over North America: Meteorological aspects and projections for the twenty-first century. *J. Climate*, **25,** 4761–4784.

L'Heureux, M. L., S. Lee, and B. Lyon, 2013: Recent multidecadal strengthening of the Walker circulation across the tropical Pacific. *Nat. Climate Change*, **3,** 571–576.

Lorenz, R., E. B. Jaeger, and S.I. Seneviratne, 2010: Persistence of heat waves and its link to soil moisture Memory. *Geophys. Res. Let.*, **37,** L09703.

Lyon, B., and R. M. Dole, 1995: A diagnostic comparison of the 1980 and 1988 U.S. summer heat wave–droughts. *J. Climate*, **8,** 1658–1676.

McCabe, G. J., M. A. Palecki, and J. L. Betancourt, 2004: Pacific and Atlantic Ocean influences on multidecadal drought frequency in the United States. *Proc. Nat. Acad. Sci.*, **101,** 4136–4141.

McGregor, S., A. Timmermann, M. F. Stuecker, M. H. England, M. Merrifield, F.-F. Jin, and Y. Chikamoto, 2014: Recent Walker circulation strengthening and Pacific cooling amplified by Atlantic warming. *Nat. Climate Change*, **4,** 888–892.

Meehl, G. A. and C. Tebaldi, 2004: More intense, more frequent, and longer lasting heat waves in the 21st century. *Science*, **305,** 994–997.

Mueller, B., and S. Seneviratne, 2012: Hot days induced by precipitation deficits at the global scale. *Proc. Natl. Acad. Sci. USA*, **109,** 12398–12403.

Nielsen-Gammon, J., 2012: The 2011 Texas drought. *Texas Water J.*, **3,** 59–95.

Peterson, T. C., and Coauthors, 2013: Monitoring and understanding changes in heat waves, cold waves, floods, and droughts in the United States: State of knowledge. *Bull. Amer. Meteor. Soc.*, **94,** 821–834.

Petoukhov, V., S. Rahmstorf, S. Petri, and H. J. Schellnhuber, 2013: Quasiresonant amplification of planetary waves and recent Northern Hemisphere weather extremes. *Proc. Nat. Acad. Sci.*, **110,** 5336–5341.

Rayner, N. A., and Coauthors, 2003: Global analyses of sea surface temperature, sea ice, and night marine air temperature since the late nineteenth century. *J. Geophys. Res.*, **108,** 4407.

Rupp, D. E., P. W. Mote, N. Massey, C. J. Rye, R. Jones, and M. R. Allen, 2012: Did human influence on climate make the 2011 Texas drought more probable? *Bull. Am. Meteorol. Soc.*, **93,** 1041–1067.

Rupp, D. E., P. W. Mote, N. Massey, F. E. L. Otto, and M. R. Allen, 2013: Human influence on the probability of low precipitation in the Central United States in 2012. *Bull. Am. Meteorol. Soc.*, **94,** S2–S6.

Rupp, D. E., S. Li, N. Massey, S. N. Sparrow, P. W. Mote, and M. R. Allen, 2015: Anthropogenic influence on the changing likelihood of an exceptionally warm summer in Texas, 2011. *Geophys. Res. Lett.*, **42,** 2392–2400.

Rupp, D. E., S. Li., P. W. Mote, N. Massey, S. N. Sparrow, and D. C. H. Wallom, 2017: Influence of the ocean and greenhouse gases on severe drought likelihood in the central US in 2012. *J. Climate*, **30,** 1789–1806.

Schär, C., D. Lüthi, and U. Beyerle, 1999: The soil-precipitation feedback: A process study with a regional climate model. *J. Climate*, **12,** 722–741.

Schneider, U., and coauthors, 2014: GPCC's new land surface precipitation climatology based on quality-controlled in situ data and its role in quantifying the global water cycle. *Theor. Appl. Climatol.*, **115,** 15–40.

Schubert, S. D., M. J. Suarez, P. J. Pegion, R. D. Koster, and J. T. Bacmeister, 2004: On the cause of the 1930s Dust Bowl. Science, 303, 1855–1859, doi:https://doi.org/10.1126/science.1095048.

Schubert, S., D. Gutzler, and Coauthors, 2009: A US CLIVAR Project to Assess and Compare the Responses of Global Climate Models to Drought-Related SST Forcing Patterns: Overview and Results. *J. Climate*, **22,** 5251–5272.

Screen, J. A., and I. Simmonds, 2014: Amplified mid-latitude planetary waves favour particular regional weather extremes. *Nat. Climate Change*, **4,** 704–709.

Seager, R., and M. Hoerling, 2014: Atmosphere and ocean origins of North American droughts. *J. Climate,* **27,** 4581–4606.

Seager, R., and M. Ting, 2017: Decadal drought variability over North America: mechanisms and predictability. *Cur.r Climate Change Rep.*, **3,** 141–149.

Smith, T. T., B. F. Zaitchik, and J. M. Gohlke, 2013: Heat waves in the United States: definitions, patterns and trends. *Climate Change*, **118,** 811–825.

Teng, H., G. Branstator, H. Wang, G. Meehl, and W. Washington, 2013: Probability of US heat waves affected by a subseasonal planetary wave pattern. *Nat. Geosci.*, **6,** 1056–1061.

Teng, H., G. Branstator, G. A. Meehl, and W. M. Washington, 2016: Projected intensification of subseasonal temperature variability and heat waves in the Great Plains. *Geophys. Res. Lett.*, **43,** 2165–2173.

Trenberth, K. E., and J. T. Fasullo, 2012: Climate extremes and climate change: The Russian heat wave and other climate extremes of 2010. *J. Geophys. Res.*, **117,** D17103.

Wang, H., S. Schubert, R. Koster, Y.-G. Ham, and M. Suarez, 2014: On the role of SST forcing in the 2011 and 2012 extreme U.S. heat and drought: A study in contrasts. *J. Hydrometeor*, **15,** 1255–1273.

Williams, P. A., and Coauthors, 2013: Temperature as a potent driver of regional forest drought stress and tree mortality. *Nat. Climate Change*, **3,** 292–297.

Wood, E. F., S. D. Schubert, A. W. Wood, C. D. Peters-Lidard, K. C. Mo, A. Mariotti, and R. S. Pulwarty, 2015: Prospects for advancing drought understanding, monitoring and prediction. *J. Hydrometeor.*, **16,** 1636–1657.

Yin, D., M. L. Roderick, G. Leech, F. Sun, and Y. Huang, 2014: The contribution of reduction in evaporative cooling to higher surface air temperatures during drought. *Geophys. Res. Lett.*, **41,** 7891–7897.

Zhang, K., T.-H. Chen, and C. E. Begley, 2015: Impact of the 2011 heat wave on mortality and emergency department visits in Houston, *Texas. Environ. Health*, **14,** 11.

Zhou, S., M. L'Heureux, S. Weaver, and A. Kumar, 2012: A composite study of the MJO influence on the surface air temperature and precipitation over the continental United States. *Climate Dyn.*, **38,** 1459–1471.

Zhou, W., S. Ji, T. H. Chen, Y. Hou, and K. Zhang, 2014: The 2011 heat wave in greater Houston: Effects of land use on temperature. *Environ. Res. Lett.*, **2014,** 135.

Figure Captions

Figure 1. (a) Climatological maximum 2-m temperature (Mx2t) and 500-hPa geopotential height (H500, unit: m). (b) Total summer extreme heat wave (EHW) days (EHWD) over the period of 1979–2015. (c) Linear trends in EHWD. The blue box in (c) outlines the Texas area (105°W–90°W, 28°N–38°N). Variables in (a)–(c) are obtained from ERA-I product.

Figure 2. (a) Light blue curve and grey bar indicate the 90^{th} and 95^{th} percentile EHWDs, respectively. The dashed curve denotes the 10-year running mean of the 90^{th} percentile EHWD. The 10 EHW years (1980, 1986, 1989, 1996, 1998, 2000, 2006, 2009, 2011, and 2012) are marked. (b) Niño3.4 index (shading, NOAA-ERv4: °C) and Texas precipitation (green: GPCC; cyan: ERA-I: $mm \cdot month^{-1}$) from January 1979 to December 2015, each of the 10 EHWs is indicated by black triangle. (c) Mx2t (shading) and its 95^{th} percent threshold (curve) at a site within Texas State, based on ERA-I product.

Figure 3. (a) Probability density function of Texas summer daily Mx2t (ERA-I). The red and grey curves respectively indicate the 10 EHW years and the rest 27 years; the blue and cyan curves respectively indicate the early period (1980–1997) and the late period (1998–2015). (b) Diagrams between Texas summer Mx2t and EHWD. The red dots indicate the 10 EHW years.

Figure 4. Composites of SSTA (NOAA-ERv4: °C) and H200 (ERA-I: m) for the antecedent winter (DJF), antecedent spring (MAM) and simultaneous summer (JJA) with respect to the 10 EHW years. Shading denotes the areas that exceed the 90% confidence level. The Texas area is marked in the right panels by a red box.

Figure 5. Composites of precipitation (shading, GPCC, unit: $mm \cdot month^{-1}$) and vertical

integrals of water vapor flux (vector, ERA-I, units: $kg{\cdot}m^{-1}{\cdot}s^{-1}$) for the antecedent spring (a) and the simultaneous summer (b) with respect to the 10 EHW years. For precipitation, the negative anomalies exceeding the 95% confidence level is stippled.

Figure 6. (a) the Pacific zonal SST gradient (PZSSTG) and (b) -Niño3.4 index, which have been normalized. (c) and (e) show the diagrams between normalized Texas spring and summer precipitations and the PZSSTG, respectively, while (d) and (f) display the diagrams between normalized Texas spring and summer precipitations and the -Niño3.4, respectively. The red dots/black crosses in (e) and (f) indicate the 2011 EHW case.

Figure 7. Same as Fig. 6, except for (a)–(b) normalized Texas soil water (blue: CPC; cyan: ERA-I) and (c)–(d) normalized Texas Mx2t (purple: NCEP2; green: ERA-I). Soil water is averaged over 0–200 cm layers. Correlation coefficients between Texas soil water from CPC and PZSSTG/-Niño3.4 from NOAA-ERAv4 are given in (c)–(f).

Figure 8. Heterogeneous correlation coefficients (CC) for the first SVD mode between outgoing longwave radiation (OLR) and EHWD. (a) CCs of OLR (shading) and SST (contour) with the time series of EHWD. (b) CC of EHWD with the time series of OLR. The explained covariance is printed at the headlines. (c) Normalized OLR (blue) and EHWD (red) time series and the linear trend in OLR (black). The square box in (a) outline the western Pacific (WP) domain (100°E–135°W, 15°S–20°N) used to define a WP OLR index next.

Figure 9. (a) Normalized WP OLR index (black curve, downward trend indicated by blue line) and NOAA-ERv4 PZSSTG (bar, upward trend indicated by red line). (b) Regression of spring H200 (ERA-I, units: m) onto -WP OLR index. (c) Same as (b), except for removing

the Niño3.4 signals from the WP OLR index. Shadings in (b) and (c) indicate the areas exceeding the 95% confidence level. Letters L and H denote the anomalous low- and high-pressure centers, respectively.

Figure 10. Normalized precipitation (a) and 2-m air temperature (T2m) (b) over Texas area during the boreal summer, which are obtained from each AGCM simulation (color solid) and observations (blue dashed). The observational precipitation (GPCC) and Mx2t (ERA-I) have been multiplied by a factor of 0.5 to match the model simulations. (c) Diagrams between normalized Texas precipitation and T2m from each AGCM simulation (dots). The multi-model mean (MMM) is indicated by black curves in (a)–(b) and black crosses in (c).

Figure 11. Left panels: Regression maps of the AGCM H200 (MAM, unit: m) onto PZSSTG (DJF). Right panels: Similar to the left, except for removing the Niño3.4 signals from the PZSSTG by linear regression. Areas exceeding the 95% confidence level are shaded.

Figure 12. Left panels: Diagrams between DJF PZSSTG and the following season's precipitation and T2m over the Texas area, where these values have been normalized. Right panels: Similar to the left, except for the -Niño3.4 index. Each model is marked by one specific color, and the MMM is indicated by black crosses. Correlation coefficients of MMM precipitation and T2m with the PZSSTG/-Niño3.4 index are given.

List of Figures

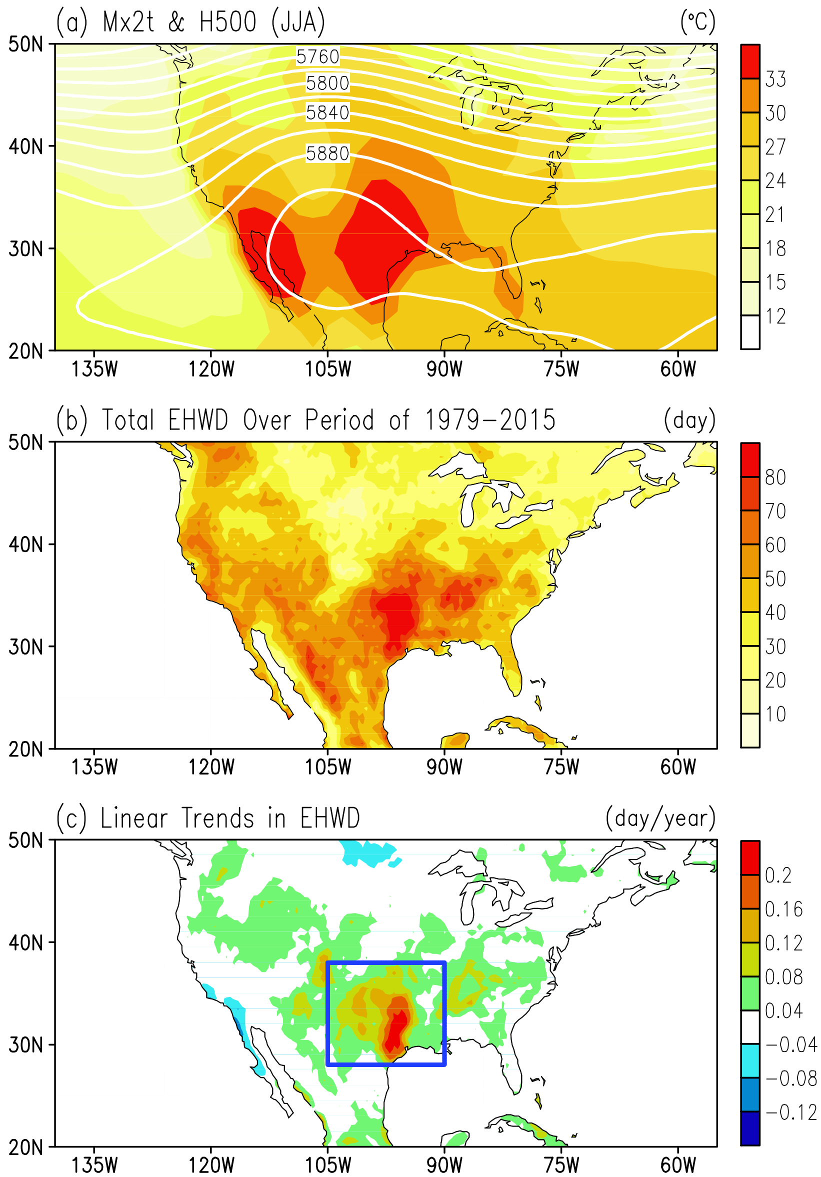

Figure 1. (a) Climatological maximum 2-m temperature (Mx2t) and 500-hPa geopotential height (H500, unit: m). (b) Total summer extreme heat wave (EHW) days (EHWD) over the period of 1979–2015. (c) Linear trends in EHWD. The blue box in (c) outlines the Texas area (105°W–90°W, 28°N–38°N). Variables in (a)–(c) are obtained from ERA-I product.

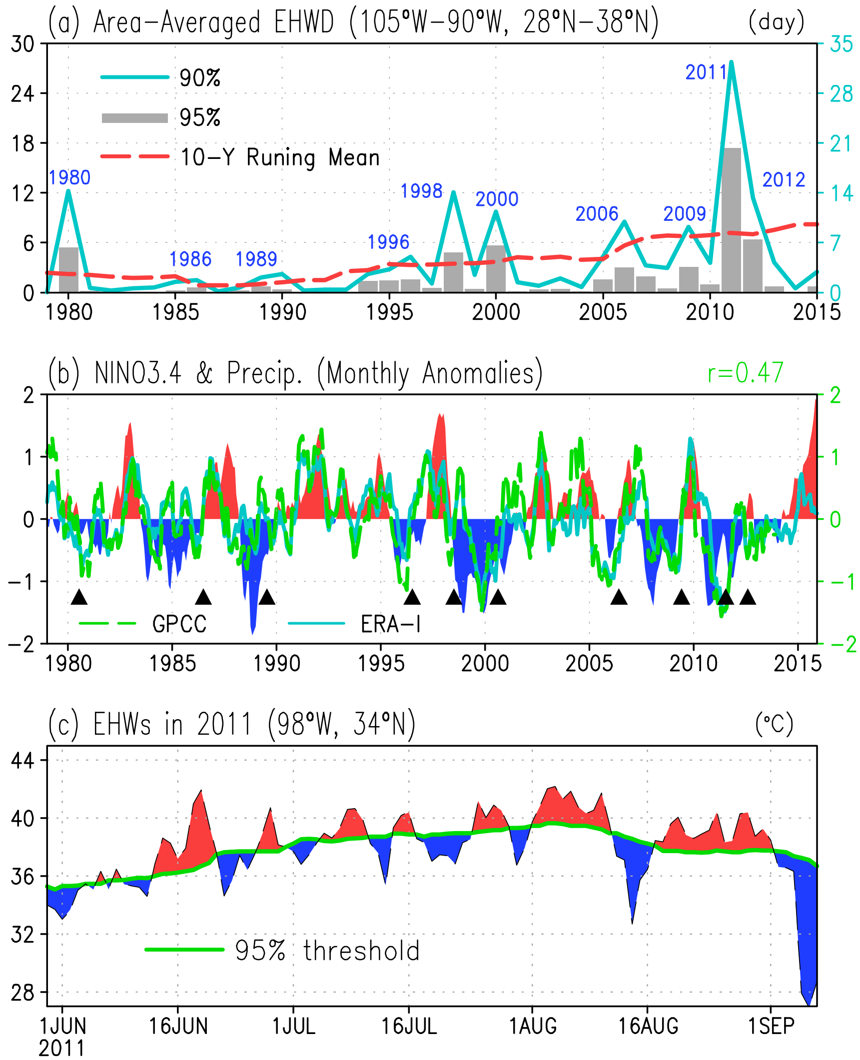

Figure 2. (a) Light blue curve and grey bar indicate the 90th and 95th percentile EHWDs, respectively. The dashed curve denotes the 10-year running mean of the 90th percentile EHWD. The 10 EHW years (1980, 1986, 1989, 1996, 1998, 2000, 2006, 2009, 2011, and 2012) are marked. (b) Niño3.4 index (shading, NOAA-ERv4: °C) and Texas precipitation (green: GPCC; cyan: ERA-I, unit: mm·month^{-1}) from January 1979 to December 2015, each of the 10 EHWs is indicated by black triangle. (c) Mx2t (shading) and its 95th percent threshold (curve) at a site within Texas State, based on ERA-I product.

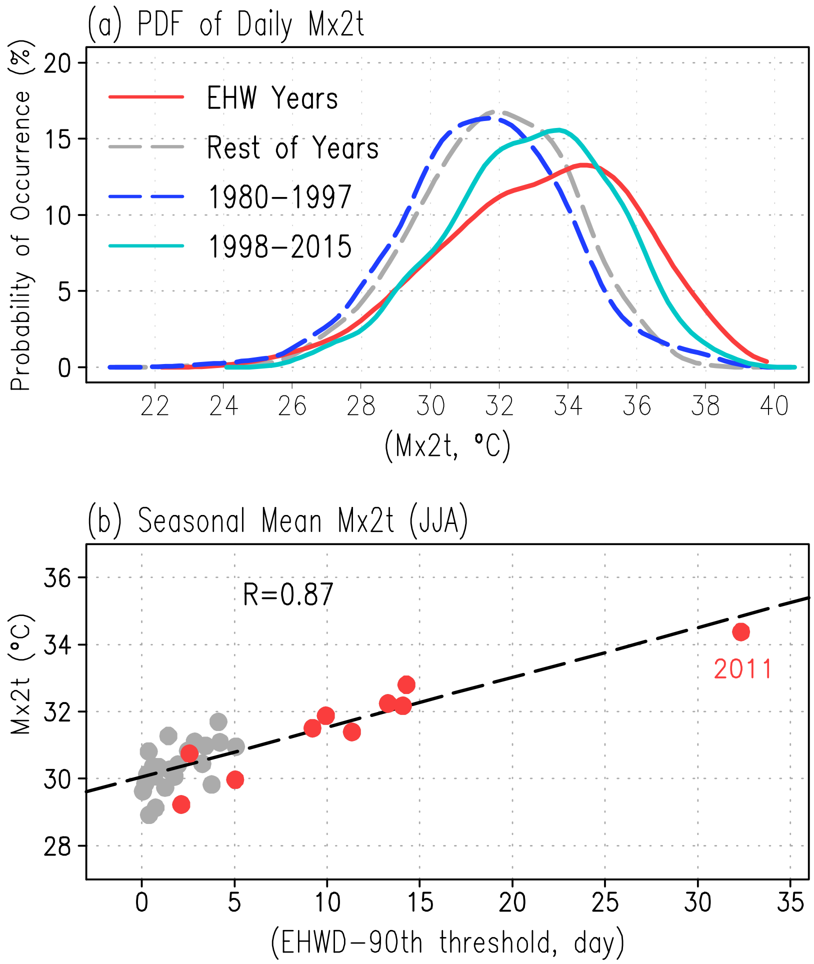

Figure 3. (a) Probability density function of Texas summer daily Mx2t (ERA-I). The red and grey curves respectively indicate the 10 EHW years and the rest 27 years; the blue and cyan curves respectively indicate the early period (1980–1997) and the late period (1998–2015). (b) Diagrams between Texas summer Mx2t and EHWD. The red dots indicate the 10 EHW years.

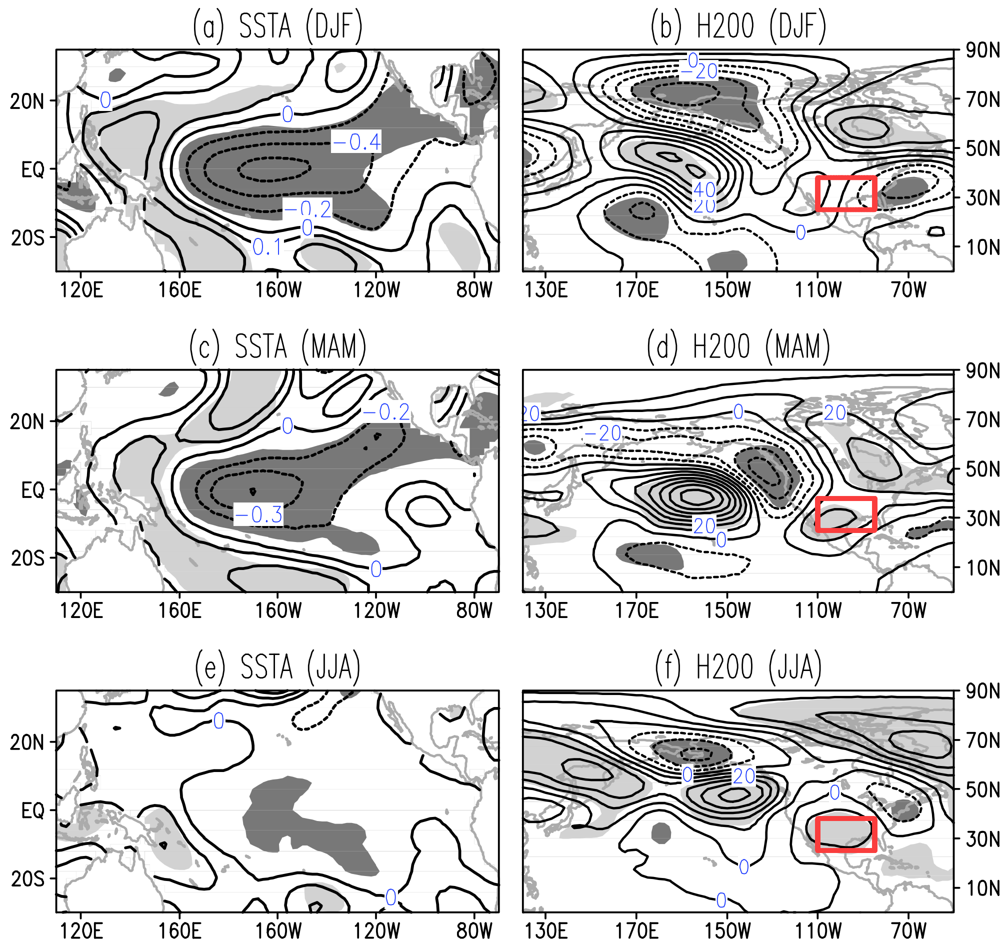

Figure 4. Composites of SSTA (NOAA-ERv4: °C) and H200 (ERA-I: m) for the antecedent winter (DJF), antecedent spring (MAM) and simultaneous summer (JJA) with respect to the 10 EHW years. Shading denotes the areas that exceed the 90% confidence level. The Texas area is marked in the right panels by a red box.

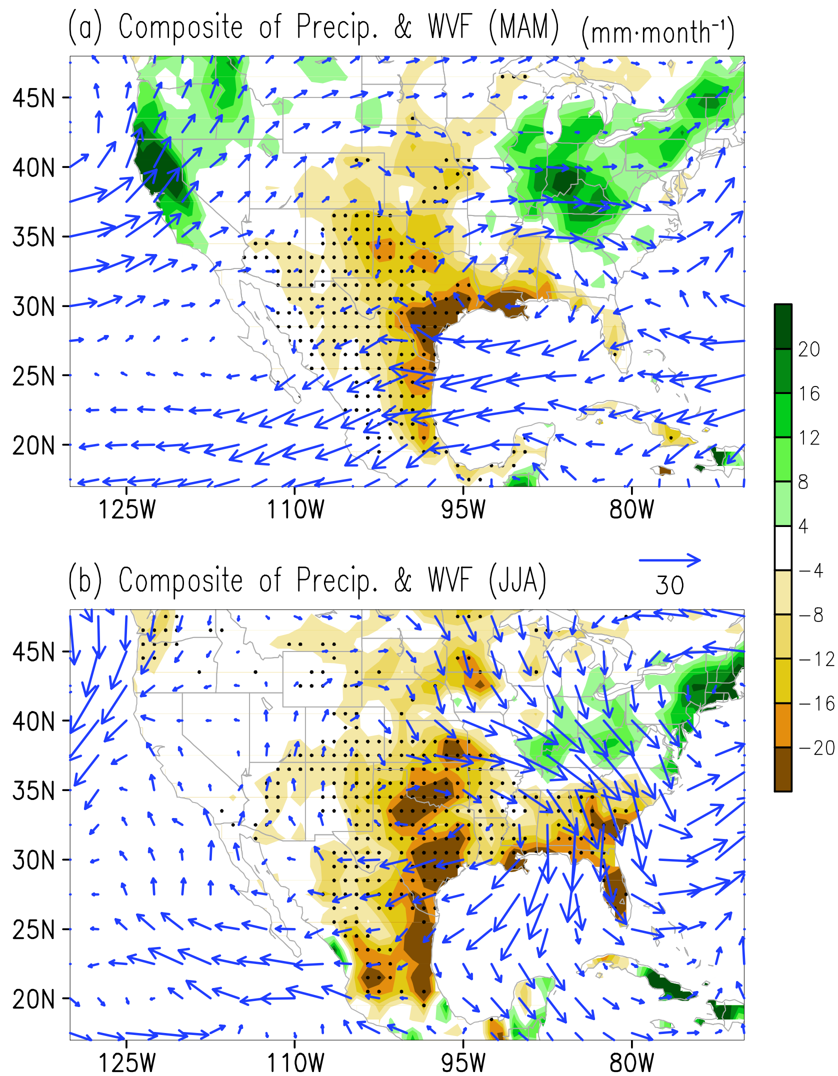

Figure 5. Composites of precipitation (shading, GPCC, unit: mm·month^{-1}) and vertical integrals of water vapor flux (vector, ERA-I, unit: kg·m^{-1}·s^{-1}) for the antecedent spring (a) and the simultaneous summer (b) with respect to the 10 EHW years. For precipitation, the negative anomalies exceeding the 95% confidence level is stippled.

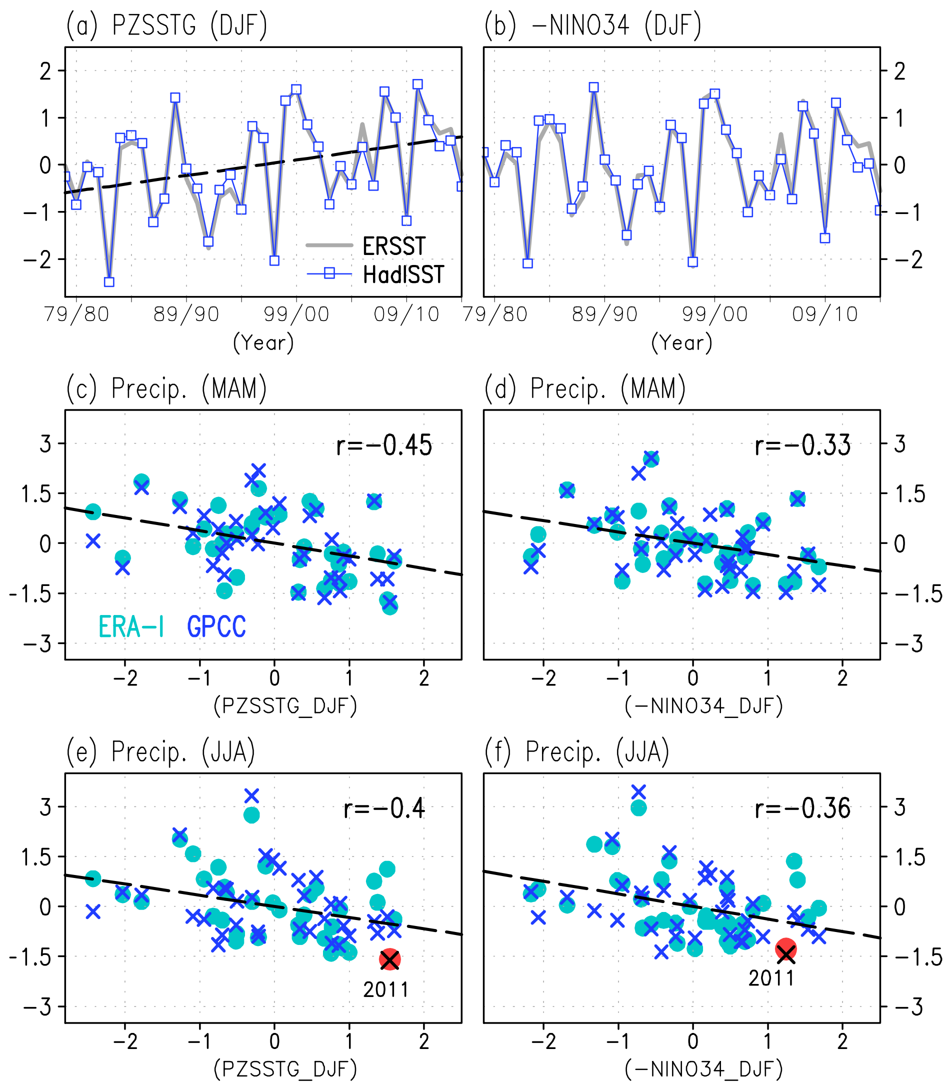

Figure 6. (a) the Pacific zonal SST gradient (PZSSTG) and (b) -Niño3.4 index, which have been normalized. (c) and (e) show the diagrams between normalized Texas spring and summer precipitations and the PZSSTG, respectively, while (d) and (f) display the diagrams between normalized Texas spring and summer precipitations and the -Niño3.4, respectively. The red dots/black crosses in (e) and (f) indicate the 2011 EHW case.

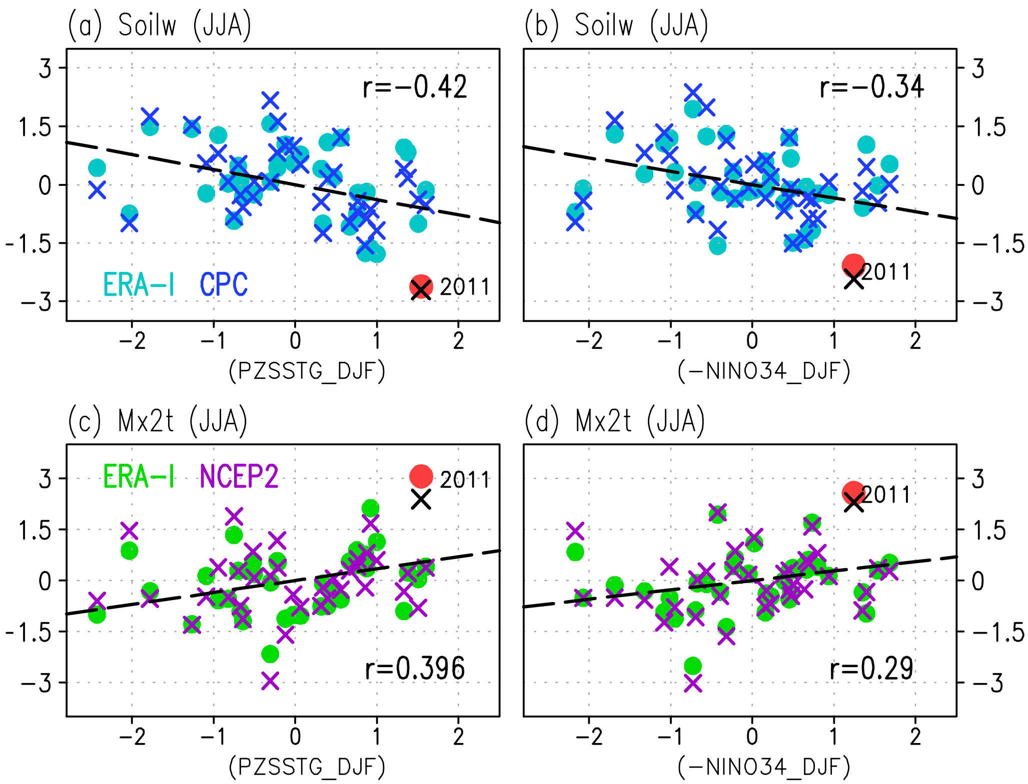

Figure 7. Same as Fig. 6, except for (a)–(b) normalized Texas soil water (blue: CPC; cyan: ERA-I) and (c)–(d) normalized Texas Mx2t (purple: NCEP2; green: ERA-I). Soil water is averaged over 0–200 cm layers. Correlation coefficients between Texas soil water from CPC and PZSSTG/-Niño3.4 from NOAA-ERAv4 are given in (c)–(f).

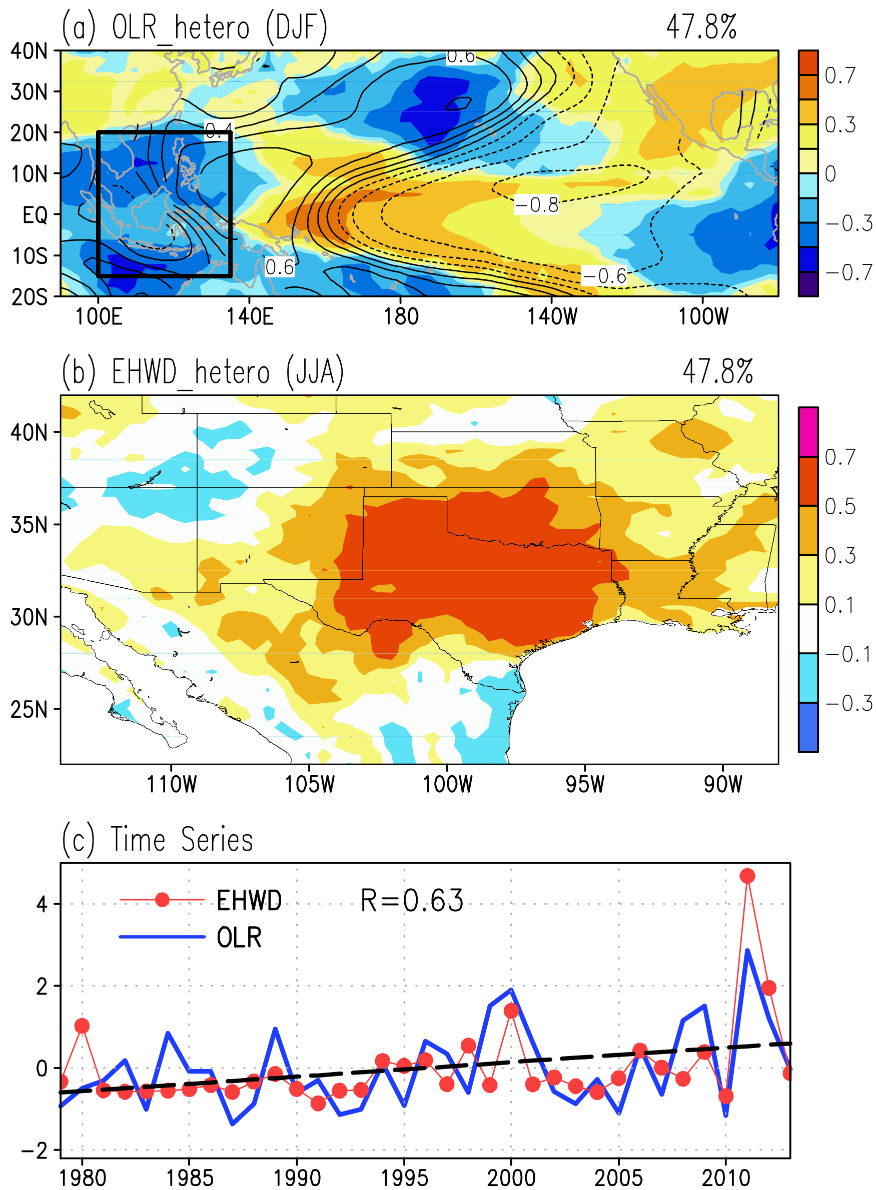

Figure 8. Heterogeneous correlation coefficients (CC) for the first SVD mode between outgoing longwave radiation (OLR) and EHWD. (a) CCs of OLR (shading) and SST (contour) with the time series of EHWD. (b) CC of EHWD with the time series of OLR. The explained covariance is printed at the headlines. (c) Normalized OLR (blue) and EHWD (red) time series and the linear trend in OLR (black). The square box in (a) outline the western Pacific (WP) domain (100°E–135°W, 15°S–20°N) used to define a WP OLR index next.

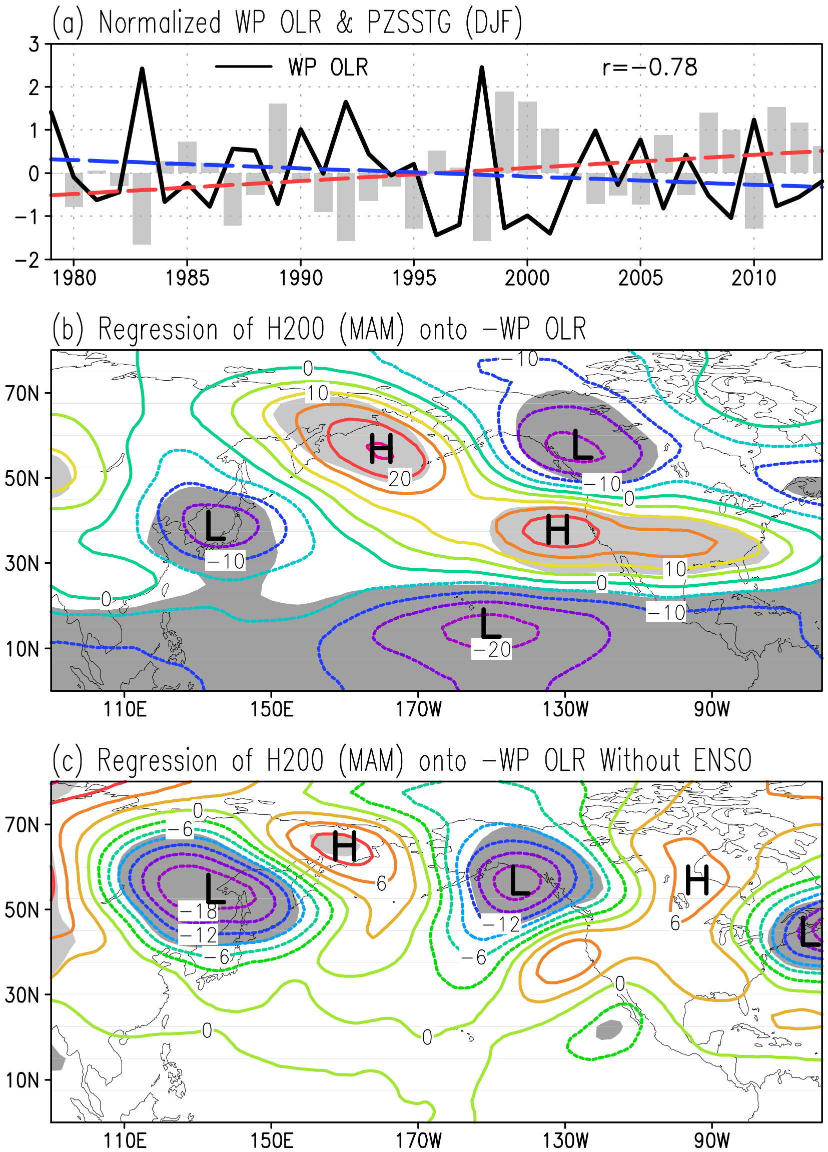

Figure 9. (a) Normalized WP OLR index (black curve, downward trend indicated by blue line) and NOAA-ERv4 PZSSTG (bar, upward trend indicated by red line). (b) Regression of spring H200 (ERA-I, units: m) onto -WP OLR index. (c) Same as (b), except for removing the Niño3.4 signals from the WP OLR index. Shadings in (b) and (c) indicate the areas exceeding the 95% confidence level. Letters L and H denote the anomalous low- and high-pressure centers, respectively.

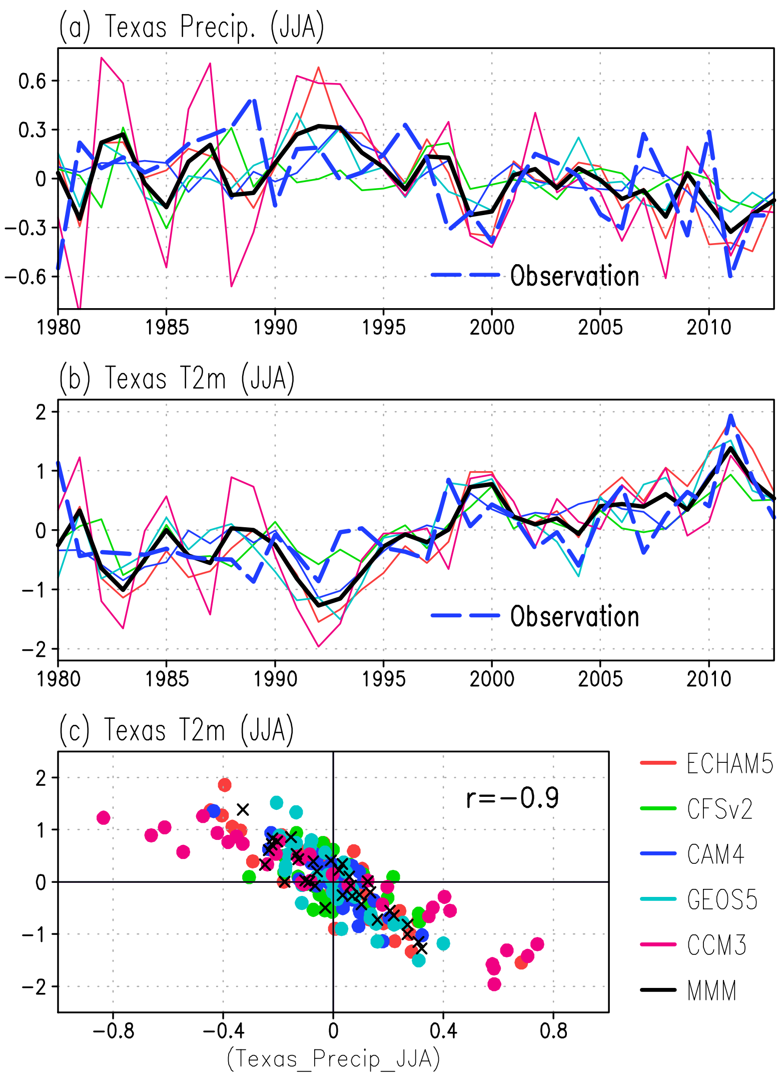

Figure 10. Normalized precipitation (a) and 2-m air temperature (T2m) (b) over Texas area during the boreal summer, which are obtained from each AGCM simulation (color solid) and observations (blue dashed). The observational precipitation (GPCC) and Mx2t (ERA-I) have been multiplied by a factor of 0.5 to match the model simulations. (c) Diagrams between Texas precipitation and T2m from each AGCM simulation (dots). The multi-model ensample mean (MMM) is indicated by black curves in (a)–(b) and black crosses in (c).

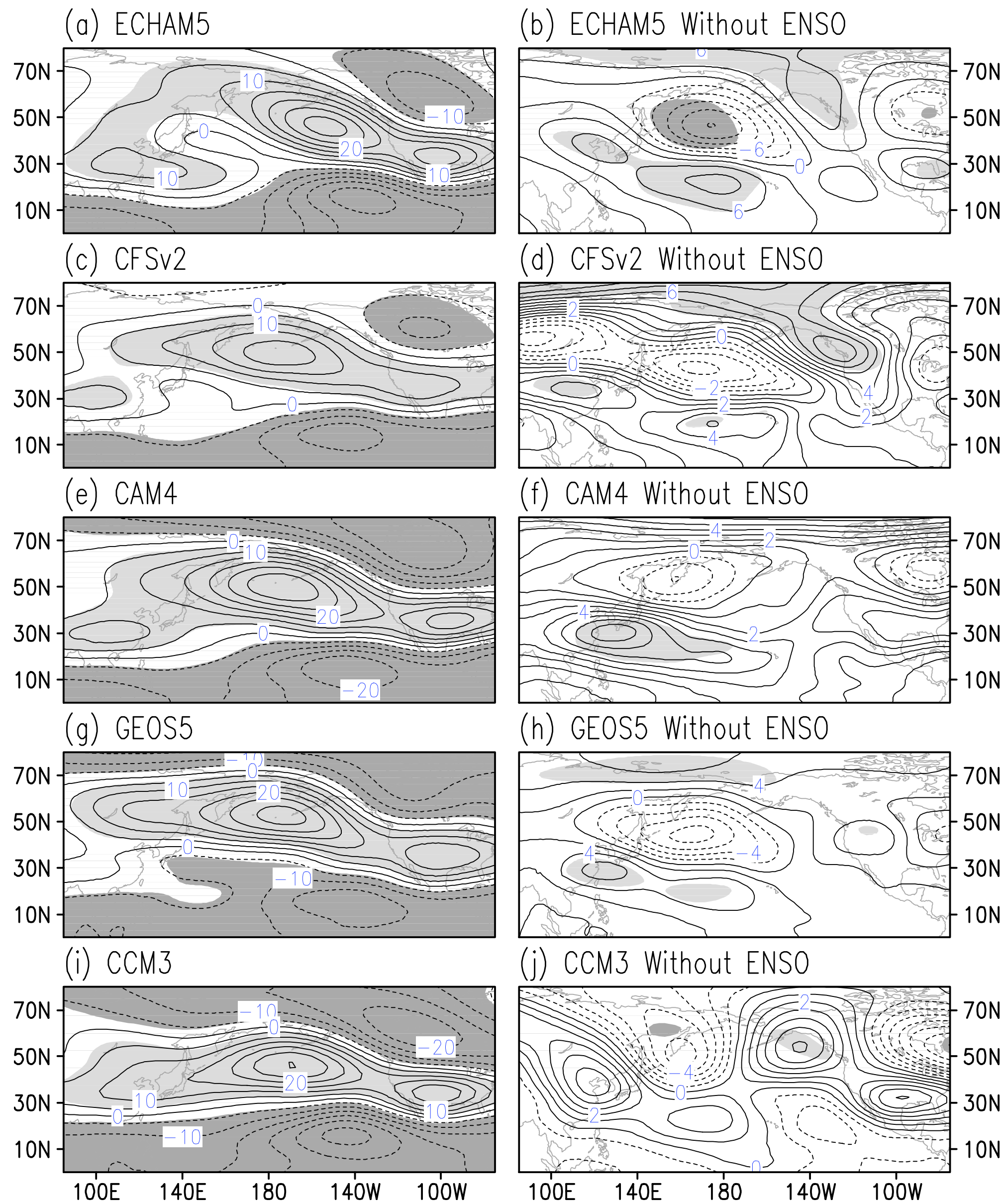

Figure 11. Left panels: Regression maps of the AGCM H200 (MAM, unit: m) onto PZSSTG (DJF). Right panels: Similar to the left, except for removing the Niño3.4 signals from the PZSSTG by linear regression. Areas exceeding the 95% confidence level are shaded.

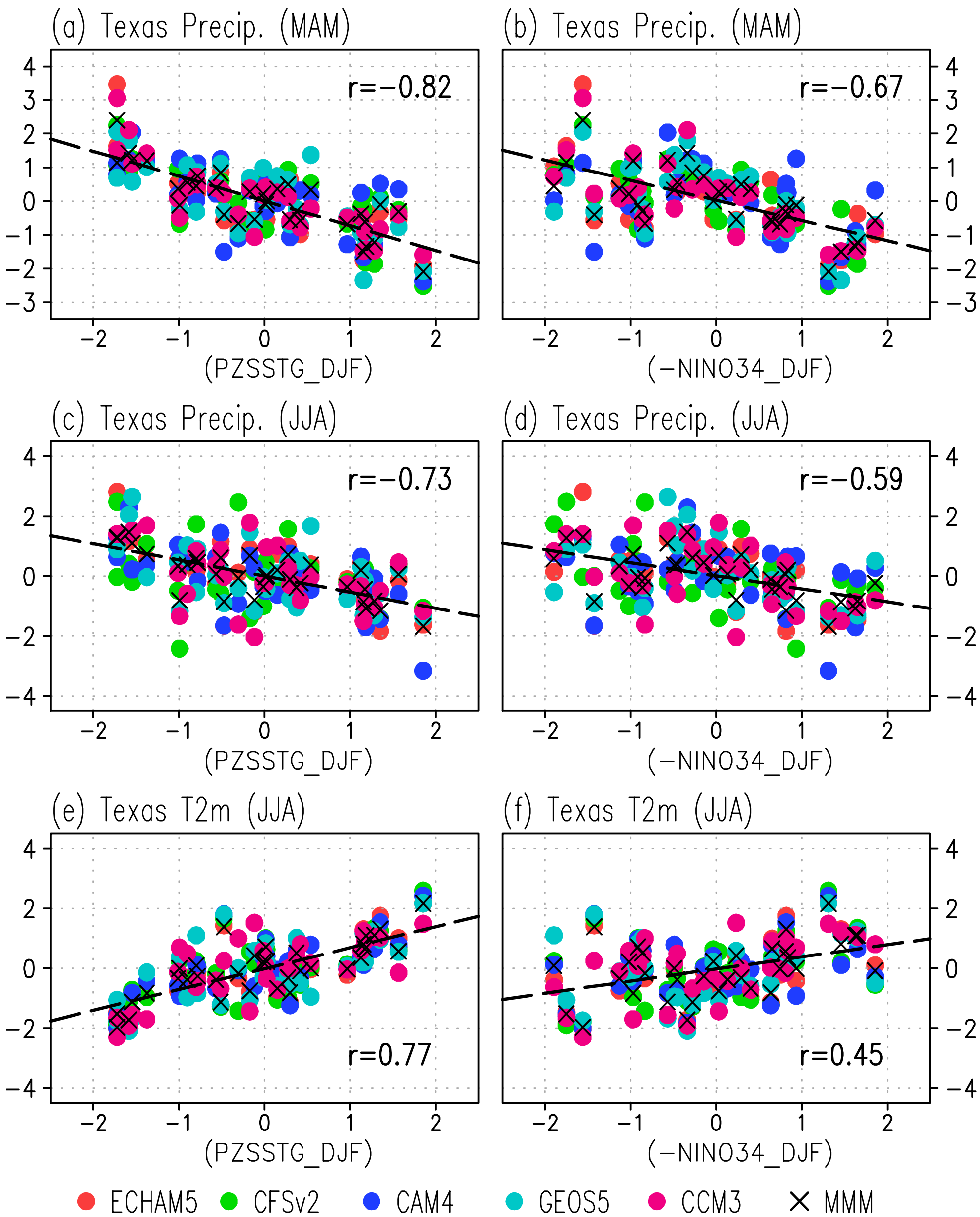

Figure 12. Left panels: Diagrams between DJF PZSSTG and the following season's precipitation and T2m over the Texas area, where these values have been normalized. Right panels: Similar to the left, except for the -Niño3.4 index. Each model is marked by one specific color, and the MMM is indicated by black crosses. Correlation coefficients of MMM precipitation and T2m with the PZSSTG/-Niño3.4 index are given.